Hyperpolarized Xe NMR signal advancement by metal-organic framework entrapment in aqueous solution

Qingbin Zeng[a,1], Binglin Bie[b,1], Qianni Guo[a,c,2], Yaping Yuan[a,c], Qi Han[b], Xiaocang Han[d], Mingwei Chen[d], Xu Zhang[a,c], Yunhuang Yang[a,c], Maili Liu[a,c], Pan Liu[d], Hexiang Deng[b,e,2], and Xin Zhou[a,c,2]

[a]Key Laboratory of Magnetic Resonance in Biological Systems, State Key Laboratory of Magnetic Resonance and Atomic and Molecular Physics, National Center for Magnetic Resonance in Wuhan, Wuhan Institute of Physics and Mathematics, Innovation Academy for Precision Measurement Science and Technology, Chinese Academy of Sciences-Wuhan National Laboratory for Optoelectronics, 430071 Wuhan, People's Republic of China; [b]Key Laboratory of Biomedical Polymers, Ministry of Education, College of Chemistry and Molecular Sciences, Wuhan University, 430072 Wuhan, People's Republic of China; [c]University of Chinese Academy of Sciences, 100049 Beijing, People's Republic of China; [d]State Key Laboratory of Metal Matrix Composites, School of Materials Science and Engineering, Shanghai Jiao Tong University, 200240 Shanghai, People's Republic of China; and [e]The Institute of Advanced Studies, Wuhan University, 430072 Wuhan, People's Republic of China

We report hyperpolarized Xe signal advancement by metal-organic framework (MOF) entrapment (Hyper-SAME) in aqueous solution. The ^{129}Xe NMR signal is drastically promoted by entrapping the Xe into the pores of MOFs. The chemical shift of entrapped ^{129}Xe is clearly distinguishable from that of free ^{129}Xe in water, due to the surface and pore environment of MOFs. The influences from the crystal size of MOFs and their concentration in water are studied. A zinc imidazole MOF, zeolitic imidazole framework-8 (ZIF-8), with particle size of 110 nm at a concentration of 100 mg/mL, was used to give an NMR signal with intensity four times that of free ^{129}Xe in water. Additionally, Hyper-SAME is compatible with hyperpolarized ^{129}Xe chemical exchange saturation transfer. The ^{129}Xe NMR signal can be amplified further by combining the two techniques. More importantly, Hyper-SAME provides a way to make detection of hyperpolarized ^{129}Xe in aqueous solution convenient and broadens the application area of MOFs.

MOFs | NMR | Hyper-CEST | MRI | signal advancement

Gas molecules are excellent probes for bioimaging using NMR techniques (1–4). This approach has great potential for non-invasive diagnosis and therapy evaluation of diseases of the respiratory system with merits unmatched by other techniques (5, 6). Among the gaseous probes, ^{129}Xe has been most widely explored and is able to provide high signal intensity through hyperpolarization. Additionally, the ^{129}Xe NMR signal intensity can be amplified through a technology called hyperpolarized Xe signal amplification by gas extraction (Hyper-SAGE) (7). However, ^{129}Xe NMR detection is not specific; if it is directly used for biological system detection, the contrast between the biological tissues and blood is usually low due to the similar chemical shifts of ^{129}Xe in these aqueous environments (8). Recently, molecular cages such as cryptophane-A (CrypA) have been successfully applied to bind hyperpolarized ^{129}Xe into its pore to give a unique chemical shift different from that of ^{129}Xe in aqueous solution (9). Coupling cryptophane with functional groups that can be tailored chemically, these molecular cages provide desirable selectivity for the imaging of target biomolecules or cells by NMR (10–15). Additionally, the captured ^{129}Xe atoms reversibly bind to cages and can be detected at ultralow concentration through hyperpolarized ^{129}Xe chemical exchange saturation transfer (Hyper-CEST) (16). However, the low solubility of these cages in aqueous solution results in limited sensitivity of the corresponding ^{129}Xe NMR signal, even when saturated aqueous solutions are used. The intensities of ^{129}Xe signals in these cages are usually less than 1/10 that of free ^{129}Xe dissolved in water (Fig. 1B); therefore, the main portion of ^{129}Xe is left unutilized. The molecular structure of these cages allows for chemical modification with hydrophilic functional groups to increase their solubility (17, 18). It remains challenging to bring up

the signal intensity to exceed that of free ^{129}Xe in water in fast and direct detection. Here, we show that the signal intensity of hyperpolarized ^{129}Xe is enhanced by hyperpolarized Xe signal advancement by metal-organic framework (MOF) entrapment (Hyper-SAME) in aqueous solution (Fig. 1). Specifically, a water-stable MOF composed of zinc and 2-methylimidazole (mIM), ZIF-8 (19, 20), was synthesized with tunable nanocrystal sizes for the optimal accommodation of Xe. The zinc ions at the framework surface provide excellent dispersity for these MOF nanoparticles in water. In addition, the hydrophobic pore environment offers specific interaction with the Xe atom, reflected in a characteristic chemical shift near 84 ppm (parts per million), which is ∼109 ppm apart from that of free ^{129}Xe in aqueous solution (near 193 ppm). The peak of entrapped ^{129}Xe is unambiguously identified, and its intensity exceeds that of free ^{129}Xe in aqueous solution (Fig. 1 A and B), leading to a high utilization rate of ^{129}Xe. The signal intensity of hyperpolarized ^{129}Xe entrapped in MOF pores, corresponding to integral, is four times stronger than that of free ^{129}Xe, 80 times stronger than that of the-state-of-the-art CrypA modified with one carboxylate group, and 200 times stronger than that of pristine

Significance

Hyperpolarized ^{129}Xe NMR/MRI is a useful method for diagnosis of diseases of the respiratory system. However, the sensitive detection of specific compounds in blood remains a challenge because of the weak ^{129}Xe signal in aqueous solution. We developed a way, Hyper-SAME, to promote the ^{129}Xe signal in aqueous solution. The ^{129}Xe signal intensity is four times beyond that of free ^{129}Xe in water and 200 times better than the benchmark molecular cage, cryptophane-A, in its saturated aqueous solution. Additionally, the hyperpolarized ^{129}Xe signal can be amplified further by combining Hyper-SAME with hyperpolarized ^{129}Xe chemical exchange saturation transfer.
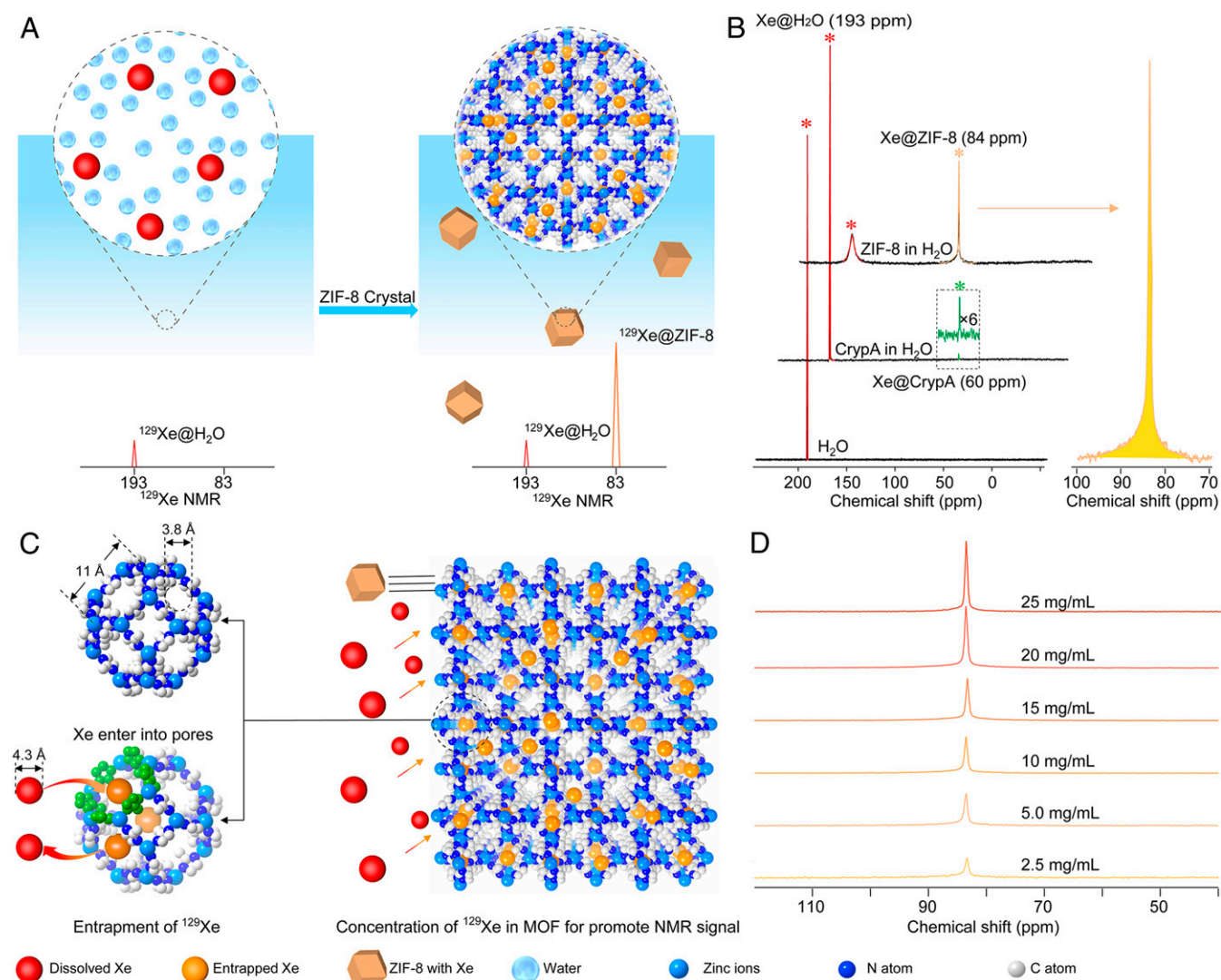
Fig. 1. Illustrations of Hyper-SAME and ^{129}Xe NMR spectra for ZIF-8 in aqueous solution. (*A*) Illustration of ^{129}Xe NMR signal enhanced by ZIF-8 in aqueous media. (*B*) NMR spectra of hyperpolarized ^{129}Xe in ultrapure water, saturated CrypA, and ZIF-8 (5.0 mg/mL) in aqueous solution. For all spectra, numbers of scan (NS) = 16, LB = 10 Hz. (*C*) Entrapment of hyperpolarized ^{129}Xe in ZIF-8 crystals. The aperture of the six-membered ring is built by six 2-methylimidazole and six zinc ions. The distance between two opposite zinc atoms is 11 Å. The diameter of the largest sphere which will pass through the window of the six-membered ring is 3.8 Å. However, the flexibility of the structure allows for an effective diameter from 3.8 Å to 4.3 Å, which is suitable for the entrance of Xe. The four-membered ring (3.2 Å) is too small for Xe atom entry and escape. Entrapped Xe is in orange and the dissolved Xe in red. (*D*) NMR spectra of hyperpolarized ^{129}Xe in ZIF-8 nanocrystals (110 nm) at different concentrations (2.5, 5.0, 10, 15, 20, and 25 mg/mL) in aqueous solution, NS = 16, LB = 10 Hz. For these ^{129}Xe NMR spectra, a zg sequence was applied for acquisition (rectangular pulse, the pulse length p1 = 31.8 μs).

CrypA, all at saturated conditions with identical volumes of water (*SI Appendix*, Figs. S28 and S29).

MOFs are porous crystalline materials constructed by metal-containing units with organic linkers (21–24) and have wide potential use in gas capture and separation (25–30), biomolecule encapsulation (31), and biomedical applications (32, 33). Gas molecules have been routinely used to study the pore environment of MOFs (19–33), with ^{129}Xe as one of the probes (34–37). However, the capability of MOFs to promote NMR signal of hyperpolarized ^{129}Xe in aqueous solution was left unexplored. Different from conventional molecular hosts used to trap Xe atoms (38–42), the high surface area and porosity of MOFs are ideally suited to concentrate Xe atoms into the pores, separating them from aqueous solution. Therefore, MOFs not only provide a unique chemical shift as a fingerprint peak for entrapped hyperpolarized ^{129}Xe but are also capable of greatly enhancing the NMR signals. In this study we demonstrated the ^{129}Xe NMR

signal amplification by MOFs. The water-soluble surface, hydrophobic pore environment, and chemical stability of ZIF-8, combined with its suitable pore size for ^{129}Xe, make it an excellent molecular host for ^{129}Xe and its NMR signal advancement in aqueous solution.

Results and Discussion

ZIF-8 nanoparticles were synthesized by mixing solutions of 2-methyl-imidazolate and zinc salts. The particle sizes of ZIF-8 were precisely controlled by reaction time and solvent types (*SI Appendix, section S1*). A series of five ZIF-8 nanoparticles with gradually increasing particle sizes, 50, 110, 120, 300, and 700 nm, were prepared with narrow size distributions, as reflected by their dynamic light scattering (DLS) analysis (*SI Appendix*, Figs. S1–S5 and Table S1). The typical dodecahedral-shaped ZIF-8 crystals were unambiguous in scanning electron microscopy (SEM) and transmission electron microscopy (TEM) images

(Fig. 2A and *SI Appendix,* Figs. S7–S10). The pores of ZIF-8 were also clearly revealed in high-resolution TEM images (*SI Appendix,* Figs. S8 and S9). Powder X-ray diffraction (PXRD) patterns of these particles matched well with the simulated pattern based on the single-crystal structure of ZIF-8, demonstrating their phase purity (*SI Appendix,* Fig. S11). Solvent molecules in the pores of ZIF-8 were removed by solvent exchange followed by exposure to vacuum. No weight loss was observed before 300 °C in the thermal gravimetric analysis (TGA) of these samples, indicating the complete removal of solvent (*SI Appendix,* Fig. S14). The permanent porosity was confirmed by the high uptake in the N_2 adsorption isotherm at 77 K. Brunauer–Emmett–Teller surface areas of these samples were around 1,400 m^2/g, and the pore size distribution was around 11 Å (*SI Appendix,* Figs. S15–S25), both consistent with previous reports (19, 20, 34).

The solvent-free ZIF-8 nanoparticles were directly used to entrap hyperpolarized ^{129}Xe in aqueous solution. A characteristic peak at 84 ppm emerged in aqueous solution with 5.0 mg/mL of ZIF-8 nanoparticles in 110-nm size (Fig. 1B). The influence of the particle size and the MOF content in the solution was investigated. We found that the entrapped ^{129}Xe NMR signal increased as more ZIF-8 with identical particle size presented in the solution, without altering the peak position (Fig. 1D). A linear relationship was established between the intensity of the entrapped ^{129}Xe NMR signal and ZIF-8 content in the range from 2.5 mg/mL to 25 mg/mL (*SI Appendix,* Fig. S30). Further increase of ZIF-8 content to 100 mg/mL led to a maximum ^{129}Xe signal intensity; however, if there was too much MOF, for example exceeding 100 mg/mL, the signal intensity did not increase any more. The impact of particle size was different from that of MOF content in aqueous solution. Not only the signal-to-noise ratio (SNR) was changed but the peak position was also different (Fig. 2B). The chemical shift of entrapped ^{129}Xe in the pores moved from 88 ppm to 82 ppm as the particle size of ZIF-8 increased from 50 nm to 300 nm (Fig. 2 B and C), while the SNR was increased by twofold (*SI Appendix,* Table S4). Further increasing the particle size to 700 nm the chemical shift of the signal was kept at 82 ppm, but the SNR slightly decreased, which could be attributed to the worse dispersity of these larger nanoparticles in water. The low dispersity of these larger nanoparticles influenced the gas capture ability of ZIF-8, which caused the NMR signal of entrapped Xe weak. We speculated that if the size of ZIF-8 was too small, the exchange between the entrapped and dissolved ^{129}Xe would be too fast, which resulted in a short relaxation time and a broad signal peak width. The ZIF-8 nanoparticle with too small size also exhibited insufficient pores to capture Xe, which also made the signal intensity weak. According to our results (*SI Appendix,* Table S4), 110 nm is the optimal particle size, considering both the SNR and peak width of entrapped ^{129}Xe in ZIF-8. Due to the gas concentration ability of ZIF-8 in aqueous solution, the ^{129}Xe entrapped in ZIF-8 with nanoparticle size of 110 nm gave the highest NMR signal intensity (signal integral), fourfold higher than that of free ^{129}Xe in aqueous solution under the same experimental conditions (*SI Appendix,* Fig. S28). This value is 200 times that of ^{129}Xe entrapped in a saturated aqueous solution of CrypA (*SI Appendix,* Fig. S29). Hyper-SAME enhanced the ^{129}Xe NMR signal through the gas
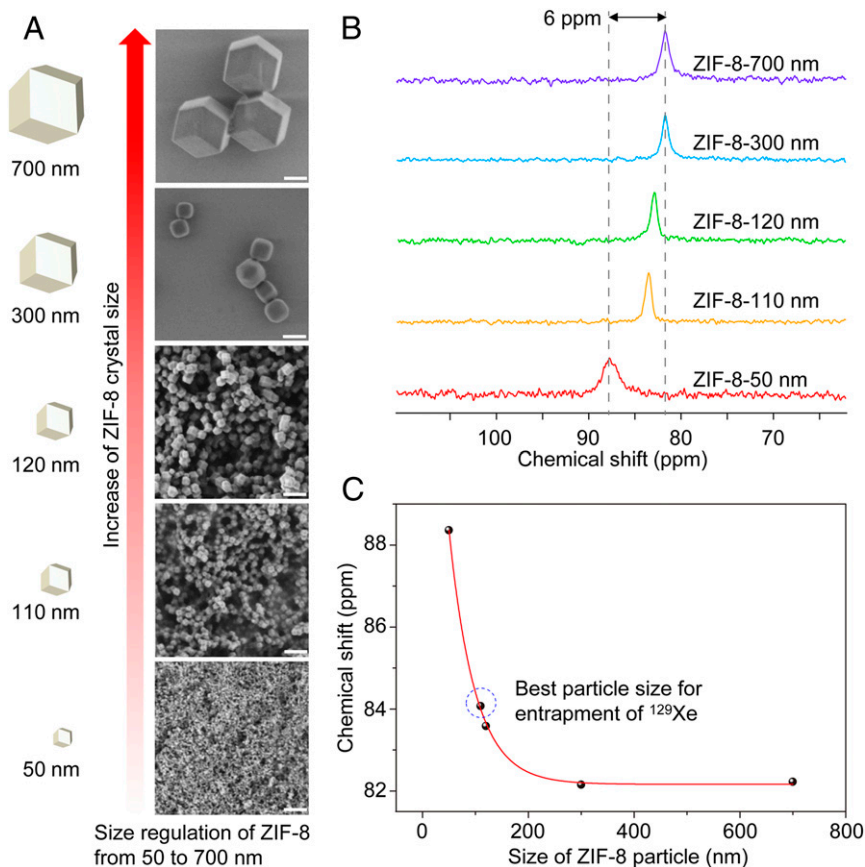

Fig. 2. SEM images and ^{129}Xe NMR spectra for different particle sizes of ZIF-8. (A) SEM images of ZIF-8 particles from 50 nm to 700 nm. (Scale bars, 200 nm.) (B) Hyperpolarized ^{129}Xe NMR spectra for different sizes of ZIF-8 (2.5 mg/mL) in aqueous solution. For these spectra, a zg sequence was applied for acquisition (rectangular pulse, the pulse length p1 = 31.8 μs). NS = 32, LB = 15 Hz. (C) The chemical shift of entrapped ^{129}Xe versus the particle size of ZIF-8 nanocrystals.

concentration ability of MOFs, which is different from Hyper-SAGE. Although the mechanism is different, the gas NMR signal promoted effect in aqueous solution of Hyper-SAME is as well as Hyper-SAGE. We can conclude that it is an efficient signal advancement strategy.

Additionally, Hyper-SAME was combined with Hyper-CEST to further amplify the NMR signal of entrapped Xe in MOF pores. When tested at a low concentration of ZIF-8 (100 μg/mL) in aqueous solution, there was no signal appearing near 84 ppm with direct detection (Fig. 3A), but two saturation responses were displayed in the Hyper-CEST spectrum (Fig. 3B). One saturation response was attributed to the direct saturation of free dissolved ^{129}Xe (center at δ = 193 ppm), whereas the other was centered at 84 ppm, arising from the saturation transfer from ^{129}Xe entrapped in ZIF-8. Although the concentration of ZIF-8 is low (100 μg/mL), the Hyper-CEST effect is ~90%, which means that the Hyper-CEST can be used to amplify the NMR signal of entrapped ^{129}Xe. Hyper-CEST MRI of ZIF-8 at low concentration (100 μg/mL) in aqueous solution was also done. The signal intensity of Hyper-CEST images is strong, and the Hyper-CEST effect is almost 65% (Fig. 3C). These results unambiguously demonstrate that the ZIF-8 is a good host for ^{129}Xe to use in hyperpolarized ^{129}Xe NMR signal advancement.

The interaction between the entrapped ^{129}Xe and the pores of ZIF-8 was studied by variable-temperature ^{129}Xe NMR experiments as well as X-ray diffraction. The chemical shift of ^{129}Xe dissolved in aqueous solution in the presence of ZIF-8 showed a nonlinear behavior (Fig. 4D), similar to that observed in pure water and in the presence of other molecular hosts. On the other hand, hyperpolarized ^{129}Xe signal entrapped in the pores of ZIF-8 exhibited a linear correlation with temperature between 278 and 320 K (Fig. 4D) and a negative slope, which was consistent with previous studies of MOFs (37, 43) but distinctively different from those in other molecular hosts (42, 44–46). Since there can be multiple Xe atoms in MOF pores, Xe–Xe interactions take place, which cannot occur relative to in the other molecular hosts with only one Xe atom per cavity (37, 44–49). At higher temperatures, the chaotic motion of Xe is more vigorous, which shortens the residence time of Xe in ZIF-8 pores and decreases the Xe–Xe interactions, leading to the upfield change in the chemical shift of entrapped ^{129}Xe in comparison to lower temperatures.

The electron density of ^{129}Xe trapped in the pores of ZIF-8 was visualized by X-ray diffraction. Difference Fourier analysis of the measured intensity profile of the ^{129}Xe-filled ZIF-8 samples was subtracted by the calculated intensity profile of pristine ZIF-8 as background, refined based on 2,242 (47 independent) reflections (Fig. 4 A and B and *SI Appendix*, Figs. S33 and S34). Although the exact atomic position of ^{129}Xe could not be determined due to disorder, the electron density map provided enough resolution to reveal the distribution of confined ^{129}Xe in the ZIF-8 pores, except for the electron density at the symmetry point of the pore center, which might be affected by termination effects in the Fourier synthesis. A large portion of the electron density was found close to the six-membered ring in ZIF-8 (Fig. 4A), while electron density is absent at the four-membered ring position (Fig. 4B). This indicates ^{129}Xe atom prefers to interact with the larger window size six-membered ring rather than the four-membered ring.

The impact of MOF pore size and pore aperture size was also studied. When an MOF with identical sod topology to ZIF-8, but with smaller pore size and aperture size, here ZIF-7, was tested on the same condition, only one peak appeared at 193 ppm representing the dissolved ^{129}Xe in water (Fig. 4C). The absence of peaks from entrapped ^{129}Xe indicated that the aperture size of ZIF-7 is too small to accommodate the Xe atom (*SI Appendix*, Fig. S35). This result demonstrates that the aperture size of ZIF-8 is just sufficient for the inclusion of Xe into its pores. The chemical shift of ^{129}Xe in a ZIF-8 solid sample was slightly different (only 2 ppm) from that in aqueous solution of ZIF-8, indicating the absence of water molecules in its hydrophobic pores.

Conclusions

In summary, we demonstrated that MOFs can be used as efficient hosts to enhance NMR signal of hyperpolarized ^{129}Xe in aqueous solution by entrapment in their pores. A maximum 200-fold improvement was observed by ZIF-8 in comparison to that of CrypA in saturated solution, while providing a unique chemical shift of 84 ppm. The favorable interaction between Xe and MOF pores, which depends on the parameters of pores and
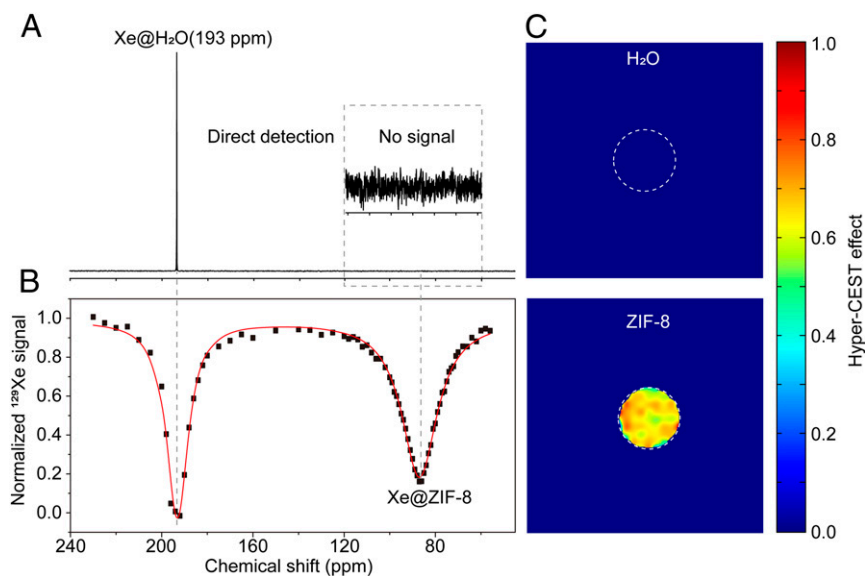

Fig. 3. Hyper-CEST NMR and MRI of ZIF-8 at low concentration in aqueous solution. (A) ^{129}Xe NMR spectra of ZIF-8 at low concentration (100 μg/mL) via direct detection method, NS = 1, LB = 5 Hz. (B) Hyper-CEST spectrum of low-concentration ZIF-8 (100 μg/mL) in H$_2$O (a 6.5-μT, 10-s saturation pulse was used). (C) Hyper-CEST MRI of low-concentration ZIF-8 (100 μg/mL) in H$_2$O. For the Hyper-CEST image, a 13-μT, 5-s saturation pulse was used. The image was acquired using a RARE sequence with 16 averages for each on- and off-resonant image.
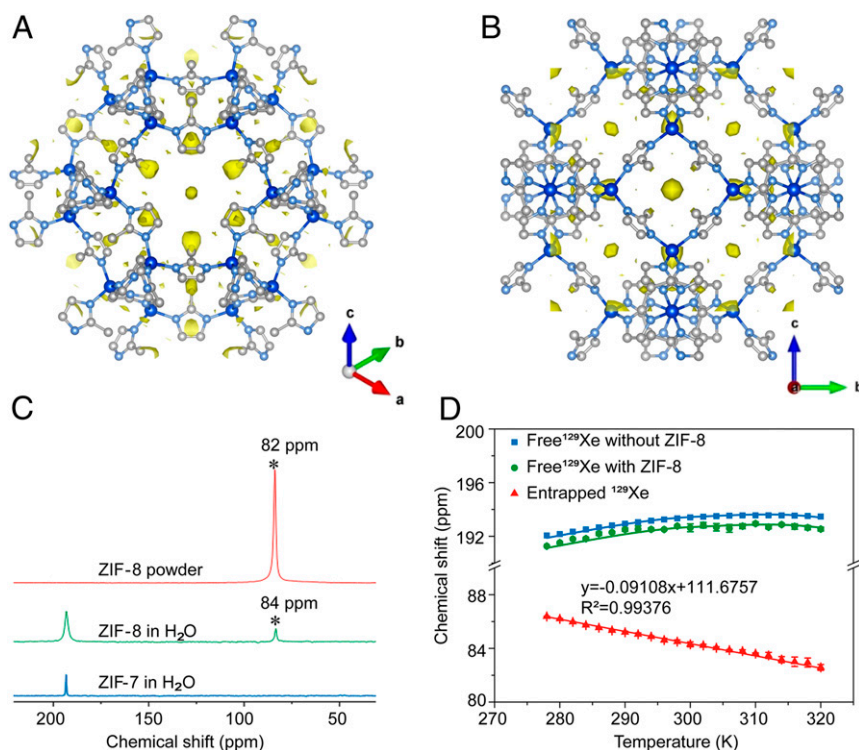
Fig. 4. X-ray diffraction of ZIF-8 filled with Xe and ^{129}Xe NMR spectra of ZIF-8 and ZIF-7. (*A* and *B*) Electron density maps of ^{129}Xe in ZIF-8 pore visualized along [111] axis (*A*) and along [100] axis (*B*). Carbon, nitrogen, and zinc atoms are in white, light blue, and dark blue, respectively. (*C*) NMR spectra of hyperpolarized ^{129}Xe interacting with ZIF-7 and ZIF-8 in aqueous solution (2.5 mg/mL) (NS = 32, LB = 40 Hz) and ZIF-8 powder (NS = 1, LB = 40 Hz). (*D*) Temperature dependence of hyperpolarized ^{129}Xe chemical shift in ZIF-8 and H$_2$O with each plot repeated in three parallel measurements. Error bars are ±SEM.

pore apertures, are critical for the signal improvement. We expected that this method could not only be applied with ZIF-8 but also be extended to more MOFs to enhance the NMR signal of gas in aqueous solution. This discovery will also help broaden the application scope of MOFs. Additionally, Hyper-SAME is also compatible with Hyper-CEST, making it a valuable tool for the detection and imaging of trace molecules in biological systems by NMR technique in the future.

Materials and Methods

Synthesis and Activation of ZIF-8. Zn(NO$_3$)$_2$·6H$_2$O (734.4 mg, 2.47 mmol) and mIM (810.6 mg, 9.87 mmol) were separately dissolved in MeOH (50 mL). The solution of mIM was poured into the solution of zinc salt under vigorous stirring. After the mixture fully mixed, the stirring was stopped immediately. Then, the white precipitate was centrifuged from the solution after standing 24 h. The residual organic linkers and metal ions in the solid were removed by washing with MeOH for three times. The pure ZIF-8 nanoparticles were dried under vacuum at room temperature and degassed in vacuum at 120 °C for 12 h. Different modulators were combined with the mIM solution to control the size of ZIF-8, as described in *SI Appendix*, section S1.

Hyperpolarized ^{129}Xe NMR. For the hyperpolarized ^{129}Xe NMR experiments, after the gas mixture polarized (home-built hyperpolarizer, hyperpolarized ^{129}Xe nuclear spin polarization was 100,000 times greater than its thermal equilibrium polarization), the gas was directly bubbled into the NMR tube containing the MOF sample (10 mm NMR) for 20 s; a delay of 3 s allowed the bubbles to collapse. A zg sequence (rectangular pulse, the pulse length p1 = 31.8 μs) was then applied to acquire the spectrum. For the variable-temperature experiments, a range of temperatures from 278 K to 320 K was used, in steps of 2 K. After a temperature stabilization time of 10 min, the ^{129}Xe NMR was obtained. For all experiments, the sample temperature was controlled by a variable temperature (VT) unit installed on the NMR spectrometer.

Hyper-CEST Spectrum. For the Hyper-CEST experiment, after the hyperpolarized gas mixture was directly bubbled into the NMR tube (10 mm NMR) for 20 s a 3-s delay time allowed the bubbles to collapse. A continuous-wave pulse (6.5 μT, 10 s) was then applied to saturate the Xe in the ZIF-8 pores, and the ^{129}Xe NMR spectrum was acquired in a single scan. Spectra were processed using Lorentzian broadening (LB = 5 Hz).

Hyper-CEST MRI. For the Hyper-CEST MRI experiment, 16 on-resonant and 16 off-resonant scans were acquired and averaged. The image was acquired using a RARE sequence (slice thickness = 30 mm, matrix size = 32 × 32, field of view = 30 × 30 mm^2, in-plane resolution = 0.9375 × 0.9375 mm^2, bandwidth = 5,400 Hz, echo time = 4.97 ms, repetition time = 82.3 ms, centric k-space encoding, no partial Fourier transform acceleration, rare factor = 8). For each excitation, the Xe gas mixture was bubbled into solution for a period of time (20 s), followed by a delay time (3 s) to allow the bubbles to collapse. After that, a saturation pulse (13 μT, 5 s) was applied to saturate the Xe in the ZIF-8 pores (−109 ppm, relative to dissolved Xe in solution at 0 ppm) or off resonance (109 ppm, relative to dissolved Xe in solution at 0 ppm). Then, the image was acquired. The MR images were processed on MATLAB (R2014a; MathWorks). The image matrix 32 × 32 was interpolated into a 128 × 128 image matrix. Hyper-CEST effect for on-resonant saturation was analyzed compared to off-resonant saturation for each pixel by the formula (CEST effect = (Intensity$_{off}$-Intensity$_{on}$)/Intensity$_{off}$) point by point.

1. M. S. Albert *et al*., Biological magnetic resonance imaging using laser-polarized [129]Xe. *Nature* **370**, 199–201 (1994).
2. M. Ebert *et al*., Nuclear magnetic resonance imaging with hyperpolarised helium-3. *Lancet* **347**, 1297–1299 (1996).
3. Z. I. Cleveland *et al*., Hyperpolarized [83]Kr MRI of lungs. *J. Magn. Reson.* **195**, 232–237 (2008).
4. X. Zhou *et al*., MRI of stroke using hyperpolarized [129]Xe. *NMR Biomed.* **24**, 170–175 (2011).
5. O. Doganay *et al*., Time-series hyperpolarized xenon-129 MRI of lobar lung ventilation of COPD in comparison to V/Q-SPECT/CT and CT. *Eur. Radiol.* **29**, 4058–4067 (2019).
6. J. M. Wang *et al*., Using hyperpolarized [129]Xe MRI to quantify regional gas transfer in idiopathic pulmonary fibrosis. *Thorax* **73**, 21–28 (2018).
7. X. Zhou, D. Graziani, A. Pines, Hyperpolarized xenon NMR and MRI signal amplification by gas extraction. *Proc. Natl. Acad. Sci. U.S.A.* **106**, 16903–16906 (2009).
8. J. P. Mugler 3rd *et al*., Simultaneous magnetic resonance imaging of ventilation distribution and gas uptake in the human lung using hyperpolarized xenon-129. *Proc. Natl. Acad. Sci. U.S.A.* **107**, 21707–21712 (2010).
9. M. M. Spence *et al*., Functionalized xenon as a biosensor. *Proc. Natl. Acad. Sci. U.S.A.* **98**, 10654–10657 (2001).
10. C. Hilty, T. J. Lowery, D. E. Wemmer, A. Pines, Spectrally resolved magnetic resonance imaging of a xenon biosensor. *Angew. Chem. Int. Ed. Engl.* **45**, 70–73 (2005).
11. J. M. Chambers *et al*., Cryptophane xenon-129 nuclear magnetic resonance biosensors targeting human carbonic anhydrase. *J. Am. Chem. Soc.* **131**, 563–569 (2009).
12. H. M. Rose *et al*., Development of an antibody-based, modular biosensor for [129]Xe NMR molecular imaging of cells at nanomolar concentrations. *Proc. Natl. Acad. Sci. U.S.A.* **111**, 11697–11702 (2014).
13. N. Kotera *et al*., A doubly responsive probe for the detection of Cys$_4$-tagged proteins. *Chem. Commun. (Camb.)* **51**, 11482–11484 (2015).
14. S. Yang *et al*., Hyperpolarized [129]Xe magnetic resonance imaging sensor for H$_2$S. *Chemistry* **23**, 7648–7652 (2017).
15. Q. Zeng *et al*., Mitochondria targeted and intracellular biothiol triggered hyperpolarized [129]Xe magnetofluorescent biosensor. *Anal. Chem.* **89**, 2288–2295 (2017).
16. L. Schröder, T. J. Lowery, C. Hilty, D. E. Wemmer, A. Pines, Molecular imaging using a targeted magnetic resonance hyperpolarized biosensor. *Science* **314**, 446–449 (2006).
17. R. Tyagi, C. Witte, R. Haag, L. Schröder, Dendronized cryptophanes as water-soluble xenon hosts for [129]Xe magnetic resonance imaging. *Org. Lett.* **16**, 4436–4439 (2014).
18. L. Delacour *et al*., "Clickable" hydrosoluble PEGylated cryptophane as a universal platform for [129]Xe magnetic resonance imaging biosensors. *Chemistry* **19**, 6089–6093 (2013).
19. K. S. Park *et al*., Exceptional chemical and thermal stability of zeolitic imidazolate frameworks. *Proc. Natl. Acad. Sci. U.S.A.* **103**, 10186–10191 (2006).
20. X. C. Huang, Y. Y. Lin, J. P. Zhang, X. M. Chen, Ligand-directed strategy for zeolite-type metal-organic frameworks: zinc(II) imidazolates with unusual zeolitic topologies. *Angew. Chem. Int. Ed. Engl.* **45**, 1557–1559 (2006).
21. H. C. Zhou, J. R. Long, O. M. Yaghi, Introduction to metal-organic frameworks. *Chem. Rev.* **112**, 673–674 (2012).
22. H. Deng *et al*., Large-pore apertures in a series of metal-organic frameworks. *Science* **336**, 1018–1023 (2012).
23. H. Deng *et al*., Multiple functional groups of varying ratios in metal-organic frameworks. *Science* **327**, 846–850 (2010).
24. X. Kong *et al*., Mapping of functional groups in metal-organic frameworks. *Science* **341**, 882–885 (2013).
25. C. Pei, T. Ben, Y. Li, S. Qiu, Synthesis of copolymerized porous organic frameworks with high gas storage capabilities at both high and low pressures. *Chem. Commun. (Camb.)* **50**, 6134–6136 (2014).
26. R. Banerjee *et al*., High-throughput synthesis of zeolitic imidazolate frameworks and application to CO$_2$ capture. *Science* **319**, 939–943 (2008).
27. L. Du *et al*., Fine-tuning pore size by shifting coordination sites of ligands and surface polarization of metal-organic frameworks to sharply enhance the selectivity for CO$_2$. *J. Am. Chem. Soc.* **135**, 562–565 (2013).
28. X. Chen *et al*., Direct observation of Xe and Kr adsorption in a Xe-selective microporous metal-organic framework. *J. Am. Chem. Soc.* **137**, 7007–7010 (2015).
29. X. Feng *et al*., Kr/Xe separation over a chabazite zeolite membrane. *J. Am. Chem. Soc.* **138**, 9791–9794 (2016).
30. P. Q. Liao, N. Y. Huang, W. X. Zhang, J. P. Zhang, X. M. Chen, Controlling guest conformation for efficient purification of butadiene. *Science* **356**, 1193–1196 (2017).
31. S. Peng *et al*., Metal-organic frameworks for precise inclusion of single-stranded DNA and transfection in immune cells. *Nat. Commun.* **9**, 1293 (2018).
32. Y. Ma *et al*., H$_2$S-activable MOF nanoparticle photosensitizer for effective photodynamic therapy against cancer with controllable singlet-oxygen release. *Angew. Chem. Int. Ed. Engl.* **56**, 13752–13756 (2017).
33. Z. Dong, Y. Sun, J. Chu, X. Zhang, H. Deng, Multivariate metal-organic frameworks for dialing-in the binding and programming the release of drug molecules. *J. Am. Chem. Soc.* **139**, 14209–14216 (2017).
34. S. Pawsey *et al*., Hyperpolarized [129]Xe nuclear magnetic resonance studies of iso-reticular metal-organic frameworks. *J. Phys. Chem. C* **111**, 6060–6067 (2007).
35. M.-A. Springuel-Huet *et al*., [129]Xe NMR study of the framework flexibility of the porous hybrid MIL-53(Al). *J. Am. Chem. Soc.* **132**, 11599–11607 (2010).
36. H. C. Hoffmann *et al*., High-pressure in situ [129]Xe NMR spectroscopy and computer simulations of breathing transitions in the metal-organic framework Ni$_2$(2,6-ndc)$_2$(dabco) (DUT-8(Ni)). *J. Am. Chem. Soc.* **133**, 8681–8690 (2011).
37. Y. Z. Chen *et al*., Location determination of metal nanoparticles relative to a metal-organic framework. *Nat. Commun.* **10**, 3462 (2019).
38. M. Kunth, C. Witte, A. Hennig, L. Schröder, Identification, classification, and signal amplification capabilities of high-turnover gas binding hosts in ultra-sensitive NMR. *Chem. Sci. (Camb.)* **6**, 6069–6075 (2015).
39. M. G. Shapiro *et al*., Genetically encoded reporters for hyperpolarized xenon magnetic resonance imaging. *Nat. Chem.* **6**, 629–634 (2014).
40. T. K. Stevens, R. M. Ramirez, A. Pines, Nanoemulsion contrast agents with sub-picomolar sensitivity for xenon NMR. *J. Am. Chem. Soc.* **135**, 9576–9579 (2013).
41. Y. Wang, B. W. Roose, E. J. Palovcak, V. Carnevale, I. J. Dmochowski, A genetically encoded β-lactamase reporter for ultrasensitive [129]Xe NMR in mammalian cells. *Angew. Chem. Int. Ed. Engl.* **55**, 8984–8987 (2016).
42. J. Roukala *et al*., Encapsulation of xenon by a self-assembled Fe$_4$L$_6$ metallosupramolecular cage. *J. Am. Chem. Soc.* **137**, 2464–2467 (2015).
43. K. J. Ooms, R. E. Wasylishen, [129]Xe NMR study of xenon in iso-reticular metal-organic frameworks. *Microporous Mesoporous Mater.* **103**, 341–351 (2007).
44. L. Schröder *et al*., Temperature response of 129Xe depolarization transfer and its application for ultrasensitive NMR detection. *Phys. Rev. Lett.* **100**, 257603 (2008).
45. G. Huber *et al*., Cryptophane-xenon complexes in organic solvents observed through NMR spectroscopy. *J. Phys. Chem. A* **112**, 11363–11372 (2008).
46. F. Schilling *et al*., MRI thermometry based on encapsulated hyperpolarized xenon. *ChemPhysChem* **11**, 3529–3533 (2010).
47. T. Ito, J. Fraissard, [129]Xe NMR study of xenon adsorbed on Y zeolites. *J. Chem. Phys.* **76**, 5225–5229 (1982).
48. H. Bunzen *et al*., Achieving large volumetric gas storage capacity in metal-organic frameworks by kinetic trapping: A case study of xenon loading in MFU-4. *J. Am. Chem. Soc.* **140**, 10191–10197 (2018).
49. T. W. Kemnitzer, C. B. L. Tschense, T. Wittmann, E. A. Rössler, J. Senker, Exploring local disorder within CAU-1 frameworks using hyperpolarized [129]Xe NMR spectroscopy. *Langmuir* **34**, 12538–12548 (2018).